Earth and Planetary Science Letters 506 (2019) 243–254

Contents lists available at ScienceDirect

Earth and Planetary Science Letters

www.elsevier.com/locate/epsl

Distributed landscape response to localized uplift and the fragility of steady states

Daniel O'Hara *, Leif Karlstrom, Joshua J. Roering

Department of Earth Sciences, 1272 University of Oregon, Eugene, OR 97403, United States of America

ARTICLE INFO

Article history:
Received 6 February 2018
Received in revised form 18 October 2018
Accepted 4 November 2018
Available online xxxx
Editor: J.P. Avouac

Keywords:
landscape evolution
divide migration
plateau formation
volcanic geomorphology

ABSTRACT

A primary goal of geomorphology is to infer from topographic form the processes that drive landscape evolution. Often implicit is the assumption that orogen-scale ($>10^{10}$ m^2 planform area) transient landscape changes on Earth are driven by equally large-scale transient tectonics, climate, or sea level. Here we argue that meso-scale (10^5–10^{10} m^2) uplift perturbations may affect landscapes on scales that far exceed their size and duration. We study the consequences of transient variations in uniform surface uplift that are localized in space, such as may occur in volcanic landscapes or during landslide emplacement. These localized uplift perturbations define a class of landforms that are larger than typical hillslope lengths but smaller than orogens, and grow at rates that are rapid compared to fluvial bedrock erosion. We use 1D and 2D landscape evolution models to show that uplift perturbations drive transient lateral migration and vertical amplification of nearby ridges, sometimes generating a spatially distributed imbalance between uplift and erosion that causes plateau-like topography. Relaxation to steady-state conditions, in which erosion balances uplift everywhere, depends on the degree to which wave-like adjustment within channels or of ridges dominates subsequent landscape erosion. We find that the spatial structure and timescales of landscape response are predictable given uplift perturbation parameters. In 2D models, localized uplift generates a radial pattern of channel network and drainage divide reorganization that remains long after the perturbation is eroded. The spatial pattern of ridges and channels in a landscape thus may record both the scale and pace of perturbations to the uplift field.

1. Introduction

Bedrock landscapes dynamically adjust in response to environmental perturbations on timescales of thousands to millions of years (e.g., Sweetkind and Blackwell, 1989). At the core of such landscape evolution is the competition between surface uplift relative to the geoid and erosion. Landscapes are in steady state (in terms of sediment flux) when rates of uplift and erosion are equal at all points on the landscape (e.g., Whipple and Tucker, 1999). Signatures of non-steady state topography are widespread and multi-scale, depending on the processes that govern uplift and erosion.

Within fluvial channels, localized convexities (knickpoints, that sometimes propagate upstream as kinematic waves, Seidl and Dietrich, 1992) record and transmit transient changes in uplift or erosion. Outside of channels, topographic adjustment occurs on hillslopes and drainage divides, and through formation of low-relief surfaces (plateaus) (Mudd and Furbish, 2005; Willett et al., 2014; Whipple et al., 2017b).

It is useful to characterize transient topography according to spatial scale. At small scales, adjustment may result from morphologic changes in soil-mantled topography caused by channel incision gradients (Mudd and Furbish, 2005), landslide thresholds (Larsen and Montgomery, 2012), or other localized processes (e.g. vegetation, climate). As spatial scale grows, the potential for transient signals to propagate from far-field sources increases: knickpoint propagation rate in fluvial channels is controlled by upstream drainage area (e.g., Lague, 2014); while drainage divides migrate in response to changes in downstream lithology (Sweeney et al., 2012), faulting (Duvall and Tucker, 2015), uplift (Willett et al., 2014), and precipitation (Bonnet, 2009).

At larger scales still, transient plateaus can record either changes in uplift that generate 'relict topography' (Whipple et al., 2017b), or changes in erosion associated with channel capture and beheading (Willett et al., 2014; Yang et al., 2015). Orogen-scale signals of landscape response to perturbations can span ~100 km^2 areas or larger (Kirby and Whipple, 2001; Braun et al., 2013). These include drainage reorganization or channel inversion asso-

* Corresponding author.
E-mail addresses: dohara@uoregon.edu (D. O'Hara), leif@uoregon.edu (L. Karlstrom), jroering@uoregon.edu (J.J. Roering).

https://doi.org/10.1016/j.epsl.2018.11.006
0012-821X/

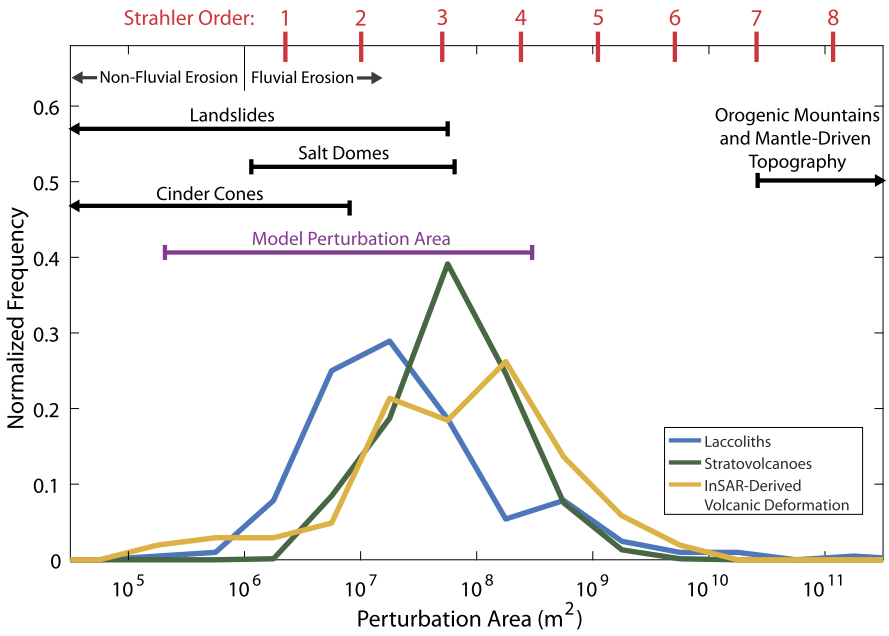

Fig. 1. The observed range of uplift scales on Earth, in terms of planform area. Colored lines show distributions of volcanic landform areas that represent a class of important meso-scale uplift perturbations. Black horizontal lines show ranges of other meso-scale perturbations and larger scale tectonic drivers. Sources listed in the text. Arrows indicate range continues beyond limit of the figure. Red vertical lines represent drainage basin areas of Strahler-order catchments for fluvial erosion. Purple horizontal line represents perturbation areas modeled in this study. (For interpretation of the colors in the figure(s), the reader is referred to the web version of this article.)

ciated with tilting or subsidence (Braun et al., 2013) and channel network disequilibrium across multiple drainage basins (Willett et al., 2014). Transience suggested by differences between local and regional slopes likely extends to continental scales (Black et al., 2017).

Many landscape evolution studies have focused on response to large-scale perturbations due to tectonics (e.g., Kirby and Whipple, 2001; Willett, 2010), mantle upwelling (e.g., Braun et al., 2013), or climate (e.g., Bonnet, 2009). These processes affect multiple catchments, as seen by comparing typical perturbation areas to average Strahler-order basin areas (Fig. 1) (Strahler, 1957; Shen et al., 2017). For example, variable tectonics affects landscape areas on the order of $\sim 10^{10}$–10^{14} m^2, at rates of $\sim 10^{-7}$–10^{-1} m/yr (Wilkinson et al., 2009).

However, not all landscape perturbations occur on large scales. Volcanism (Karlstrom et al., 2018), salt domes (Anderson et al., 1973), and landsliding (Guzzetti et al., 2009) occur on sub-catchment scales (Fig. 1). These meso-scale perturbations are likely small compared to those from mantle upwellings or tectonics, but may have a significant impact on landscape adjustment and induce feedback mechanisms due to their effect on upstream catchments and repeated occurrences in time. Such perturbations dominate land surface uplift in long-lived ($>\sim$ 1–10 Myr) volcanic terrains, which occupy roughly 10% of current land area globally (Wilkinson et al., 2009).

Understanding landscape response to such meso-scale uplift perturbations motivates this study. We use magmatic landforms as a template for the uplift perturbations. For example, laccoliths have heights ranging between ~30–9500 m with planform areas ~0.16–11000 km^2 (Fig. 1, blue line) (Gilbert, 1877; Corry, 1988). These structures form via flexure of near surface rocks due to the emplacement of shallow magmatic sills (e.g., de Saint-Blanquat et al., 2006), which may generate local uplift rates of $\sim$1–10^3 m/yr over monthly to 100 yr timescales (de Saint-Blanquat et al., 2006; Castro et al., 2016). Such perturbations are near-instantaneous compared to bedrock erosion on this spatial scale.

In what follows, we explore the response of an initially steady-state landscape to finite uplift that occurs on spatial scales smaller than a typical drainage basin. We use 1D and 2D landscape evolution models to quantify transient landscape response. We find that response can vary from simple knickpoint generation to plateau formation and basin reorganization. Upstream drainage divides adjust to uplift perturbations through lateral migration and amplification. Ridge migration velocities are well predicted by a model that integrates downstream channel and hillslope processes.

2. Methods

We develop numerical landscape evolution models in stages of increasing complexity. 1D models have one steady-state solution, simplifying transient evolution (e.g. Perron and Fagherazzi, 2012). We then develop a 2D model to illustrate similarities and differences in a system with more spatial degrees of freedom. Parameters and variables are summarized in Supplemental Table T1.

Changes in surface elevations at a point in response to uplift relative to the geoid and erosion (Molnar and England, 1990) are described by

$$\frac{\partial z}{\partial t} = u - E, \tag{1}$$

where $z = z(x, y, t)$ is elevation, $u = u(x, y, t)$ is uplift rate, $E = E(x, y, t)$ is erosion rate, x and y are spatial coordinates, and t is time. We account for both fluvial and hillslope erosion, modeling transient ridge migration within a dominantly detachment-limited fluvial setting.

2.1. Erosion laws

Fluvial bedrock erosion occurs by abrasion and plucking, induced by shear stress acting on the channel bed, and is generally described by the semi-empirical stream power law (e.g., Whipple and Tucker, 1999):

$$E = K A^M |\nabla z|^N, \tag{2}$$

where erodibility coefficient $K = K(x, y, t)$ and $A = A(x, y, t)$ is upstream drainage area. M and N are empirical exponents, with

$\frac{M}{N}$ often ~0.5 in terrestrial landscapes (Whipple and Tucker, 1999). For simplicity we assume $N = 1$ and $M = 0.5$, although this is not observed for all landscapes (Harel et al., 2016). We further assume uniform lithology and precipitation, and thus constant erodibility $K = 10^{-6}$ m^{1-2M}/yr. In many landscapes, K ranges $\sim 10^{-7}$–10^{-3} (Stock and Montgomery, 1999).

The formulation of equation (2) requires assumed relations between channel geometry (i.e. width and depth) and basin state (i.e. topology, drainage area, structural state) that are empirically-defined (Whipple and Tucker, 1999). Furthermore, use of equation (2) over all channelized portions of the landscape suggests river discharge is always large enough to both transport all sediment loads through the system and create shear stress in excess of that required for bedrock erosion (Whipple and Tucker, 1999). Despite its simplicity, the stream power law is prevalently used in landscape evolution models (e.g. Braun and Willett, 2013; Goren et al., 2014) and to derive metrics that define landscape disequilibrium (e.g. Kirby and Whipple, 2001; Royden and Perron, 2013; Willett et al., 2014). Thus, equation (2) permits exploration of localized perturbations on landscape scale without appealing to complex erosion mechanics that are under development and require challenging parameterization.

We assume soil-mantled hillslopes with gentle enough slopes that landsliding does not occur, requiring soil production rates to be in equilibrium with erosion (Roering et al., 2001). Downhill sediment flux through soil creep $\vec{q} = \vec{q}(x, y, t)$ is governed by the negative product of local slope and a diffusivity coefficient $D = D(x, y, t)$:

$$\vec{q} = -D\nabla z. \tag{3}$$

D is typically in the range of $\sim 10^{-4}$–10^{-1} m^2/yr (Hurst et al., 2013). We assume constant diffusivity (10^{-2} m^2/yr) and linear dependence of soil flux on slope,

$$E = \nabla \cdot \vec{q} = -D\nabla^2 z. \tag{4}$$

The assumption of a linear flux model is not ideally suited for rapidly uplifting tectonic settings, where hillslopes are better modeled using a non-linear flux relation (e.g. Roering et al., 2001; Mudd and Furbish, 2005). The distinction between these models are changes in hillslope relief, signal propagation speed, and sediment load entering rivers. However, we justify this simplification as 1) overall landscape relief and response time are predominately set by fluvial erosion, 2) the stream power law, as used, does not include a sediment flux term, negating the influence of hillslope sediment delivery on channel incision, and 3) the linear flux model has a simple analytic solution which keeps model results and analysis tractable.

2.2. Localized uplift

We model transient, localized uplift by parameterizing flexural solutions to thin-plate elasticity (Pollard and Johnson, 1973), mimicking structures seen in laccoliths (Corry, 1988). We assume

$$u(x, y, t) = \begin{cases} u_0 + u_P \left(1 - \left(\frac{r(x,y)}{R_P}\right)^2\right), & r \le R_P \text{ and } 0 < t \le t_P \\ u_0, & \text{else} \end{cases} \tag{5}$$

in which $r(x, y) = \sqrt{(x - x_P)^2 + (y - y_P)^2}$ is radial distance from the perturbation center (x_P, y_P), u_0 is background uplift (10^{-4} m/yr), R_P is perturbation radius, u_P is maximum perturbation uplift rate, and t_P is total perturbation uplift time. When $t > t_P$, u_0 is uniform over the entire landscape. In all models, we assume that localized uplift is confined to one basin and does not overlap spatially with initial drainage divides. This assumption is not valid in all situations of localized uplift, but allows for a simplified geometry with which to systematically track perturbation effects.

Combining (1), (2), (4) and (5) thus gives the landscape evolution equation

$$\frac{\partial z}{\partial t} = u - C_I|\nabla z| + D\nabla^2 z, \tag{6}$$

an advection–diffusion equation characterized by spatially variable wavespeed

$$C_I(x, y, t) = K A(x, y, t)^M. \tag{7}$$

We assume the advective term is active only in fluvial channels and the diffusive term only on hillslopes, as defined by a critical drainage length (Whipple and Tucker, 1999). Our use of $M = 0.5$ and $N = 1$ is a simplification that is not observed in all landscapes, as Harel et al. (2016) suggest most environments may have a mean slope exponent value greater than 1. Using an N value greater than 1 alters advection wavespeed, influencing landscape adjustment timescales (Whipple and Tucker, 1999), and introduces a dependency of erosion rate on drainage density (Tucker and Bras, 1998). Our use of $N = 1$ provides a simplified quantitative approach to analyze and explain regional landscape response to meso-scale perturbations.

2.3. 1D model

To build intuition we first analyze transient uplift in one dimension. We find numerical solutions to equation (6) by discretizing using a backwards-time, backwards-space and backwards-time, centered-space finite difference scheme for the advective and diffusion terms, respectively (Supplemental Methods). We relate drainage area to basin length using Hack's Law (Hack, 1957),

$$A = k_a x^H. \tag{8}$$

k_a and H are Hack's coefficient and exponent, respectively, and x here represents the distance from the upstream drainage divide. For simplicity, we use $k_a = 0.57$ m^{2-H} and $H = 1.67$ (Hack, 1957), implying a dendritic river system; however, these parameters likely depend on local erosion mechanics that define basin topology.

We assume a model domain of length 60 km and grid resolution 50 m, with both ends of the domain fixed at base level z_b. This implies a single steady-state solution with two catchments separated by a divide, which has an analytic solution (Fig. 2.A). We define the critical drainage length, x_c, as the inflection point between convex fluvial channels and concave hillslopes in steady state (e.g., Perron et al., 2009),

$$x_c = \left(\frac{D}{K(k_a)^M}\right)^{\frac{1}{1+HM}}. \tag{9}$$

Localized uplift sometimes generates secondary drainage divides and associated local minima (where down-slope topography converges). We assume local minima are associated with internally-drained basins and do not erode, uplifting at the background rate. Uplift continues until the internally-drained basin is the same elevation as one of the surrounding divides, at which point the divide is captured by its neighboring basin. This method of allowing local minima to act as transient features is qualitatively similar to previous models (Willett, 2010) that assumed sediment deposition fills local minima.

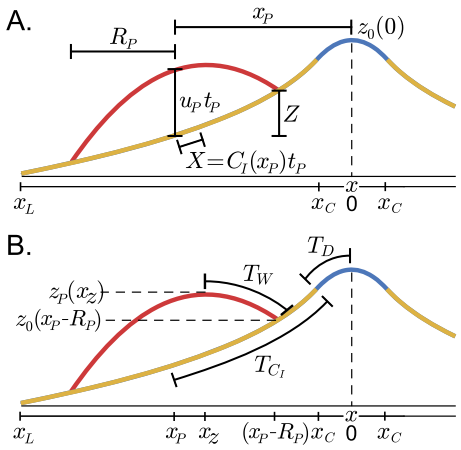

Fig. 2. 1D Model setup and symbol definition. A: Initial steady-state topography with only one drainage divide (blue and yellow lines), and perturbed topography (red line). Horizontal axis is the local spatial coordinate system. Blue line represents the domain where hillslope processes dominate (bounded by critical drainage length x_c), yellow lines represent fluvial domain. Parameters listed are geometric scales for equation (13). B: Same topography as A, illustrating the geometry of how timescales described in equations (17), (18), and (20) are calculated.

2.4. 2D model

We model landscape response in 2D using Fastscape (Braun and Willett, 2013), which solves equation (6) using an implicit finite difference scheme for fluvial and hillslope erosion. The landscape is modeled on a grid of length 60 km and resolution 150 m in both x and y with base level defined as points centered on each grid boundary face, creating four basins in steady state. Initial steady-state is found by uplifting flat topography at u_0 until mean topography is constant in time. Similar to 1D, we allow local minima to act as internally-drained basins.

2.5. Non-dimensionalization and transient response metrics

We nondimensionalize equation (6) as

$$t = t_P t^*, \quad u = u_P u^*, \quad x = X x^*, \quad y = X y^*,$$
$$A = \alpha A^*, \quad z = Z z^*, \tag{10}$$

where stars indicate dimensionless variables. Characteristic scales are defined by the perturbation maximum uplift rate (u_P) and timescale (t_P); $X = C_I(x_P, y_P)t_P$, distance upstream of the perturbation center calculated using the steady-state wavespeed implied by equation (7) evaluated at (x_P, y_P) (Fig. 2.A); $\alpha = k_a(R_P)^H$, local drainage area on the perturbation given by Hack's Law. Z is defined as initial local relief between the center and upstream edge of the perturbation (Fig. 2.A). In 1D, this is

$$Z = \frac{u_0\left((x_P)^{1-HM} - (x_P - R_P)^{1-HM}\right)}{K(k_a)^M(1-HM)}. \tag{11}$$

In 2D multiple channels and subcatchments may exist within the perturbed region, so we take this value as the relief of the highest-order channel within the constraints of the perturbation.

Substituting (10) into (6) and rearranging gives

$$\frac{\partial z^*}{\partial t^*} = \beta u^* - \eta A^{*M}|\nabla z^*| + \gamma \nabla^2 z^*, \tag{12}$$

where

$$\beta = \frac{u_P t_P}{Z}, \qquad \eta = \frac{K\alpha^M t_P}{X} = \frac{C_I(R_P)}{C_I(x_P, y_P)} = \left(\frac{R_P}{x_P}\right)^{HM},$$
$$\gamma = \frac{D t_P}{X^2}. \tag{13}$$

Nondimensional control parameters in equation (12) are simply interpreted: β compares perturbation relief to initial local relief. η is a ratio of channel wave velocities, comparing drainage area of the perturbation with that of the initial channel. γ compares perturbation uplift timescale to the hillslope diffusion timescale X^2/D.

3. Results

We analyze landscape transient response using a series of metrics and a grid search over u_P, t_P, R_P, x_P, and y_P, keeping all other parameters constant. Parameter ranges are defined by laccolith spatial scales and uplift rates (Fig. 1, purple line) (Corry, 1988; de Saint-Blanquat et al., 2006). Variable model perturbation parameters are listed in Supplemental Table T2. In total, we run 10347 1D and 25 2D models.

We focus specifically on the β–η parameter space, as little variation is observed with γ for the assumed hillslope parameters (Supplemental Fig. S3). This does not imply that hillslopes are not important, as we will demonstrate. Within the β–η space, higher perturbation uplift rates (u_P) and timescales (t_P) correspond to higher β values, and perturbations closer to the basin mouth (higher x_P) or lower perturbation sizes (R_P) correspond to both higher β and lower η values (Fig. 3.A).

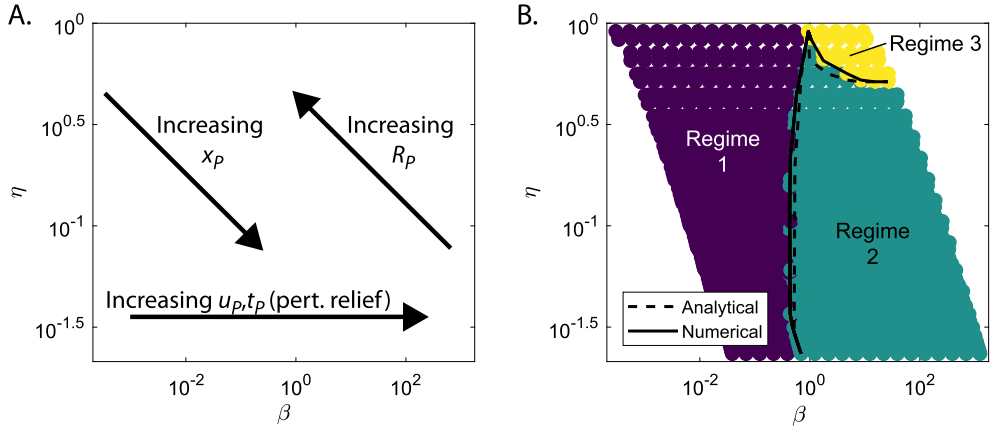

Fig. 3. A: Nondimensional space showing how dimensional perturbation parameters affect dimensionless numbers η and β. B: Grid search results showing model regimes defined in the text and described in Fig. 4. Solid black lines indicate regime boundaries. Dashed black lines show regime boundaries determined analytically, as described in the text.

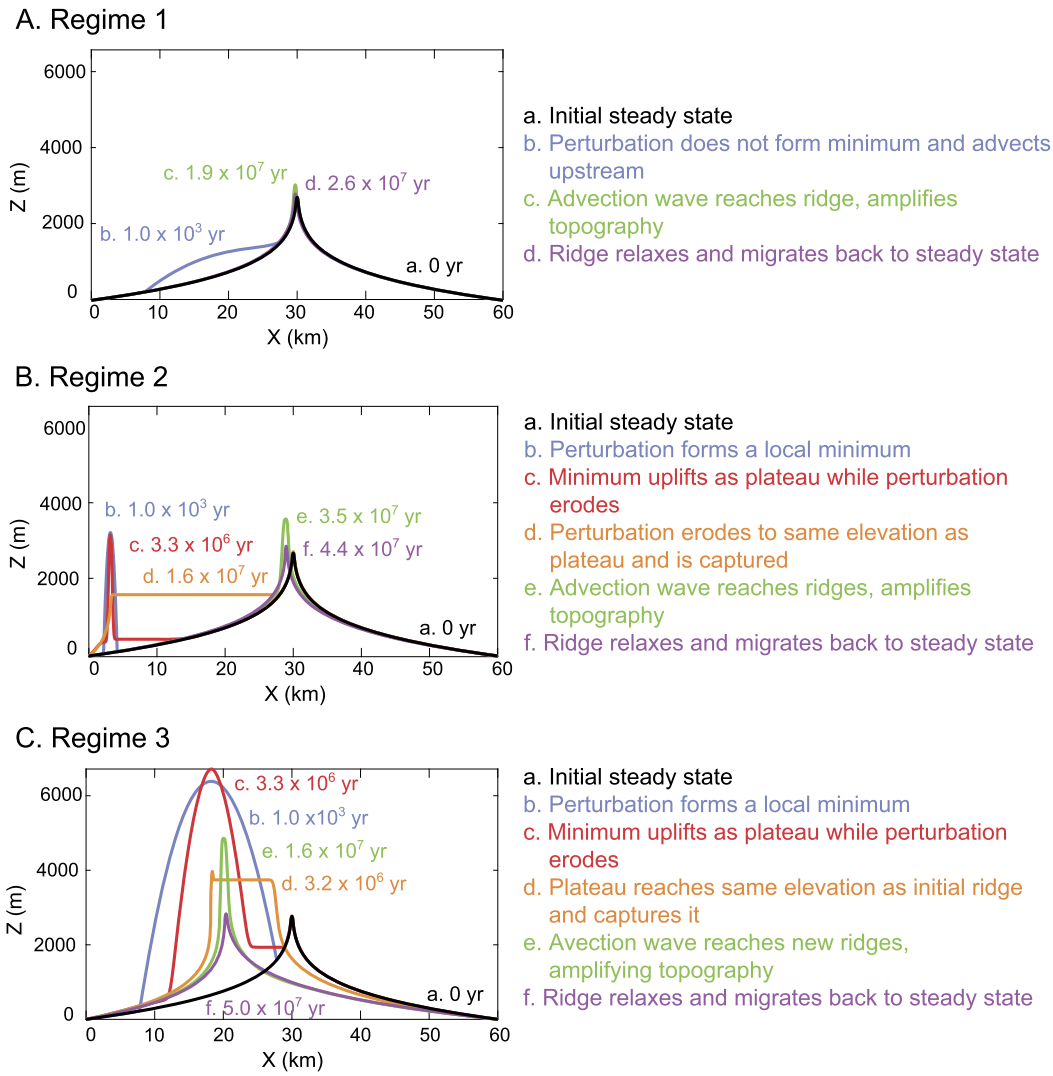

Fig. 4. Transient behavior defining the three regimes observed in 1D models. Panels show model topography, with colored lines for model times associated with significant events and associated text.

3.1. 1D models

Three regimes of transient landscape behavior are observed in 1D (Fig. 4).

Regime 1 *(No Ridge Formation (Fig. 4.A, Supplemental Movie M1)).* The perturbation creates positive topography on the landscape that is lower in relief than the initial upstream channel, and advects upstream as a knickpoint. Upon reaching the divide, the knickpoint perturbs the divide by amplifying topography and inducing lateral divide migration towards the perturbed basin. The divide then returns to its pre-perturbation steady-state position.

Regime 2 *(Initial Topography Dominates (Fig. 4.B, Supplemental Movie M2)).* The perturbation forms a new ridge and local minimum in the previously upstream channel. The local minimum is erosion-deficient and uplifts as a plateau, while headward erosion propagates upstream on both sides of the perturbation in response to channel length change. After localized uplift has stopped, the perturbation uplifts at background rate u_0 until headward erosion reaches the new ridge and erodes it. Erosion continues until the perturbation and adjoining plateau have equal elevation and the perturbation becomes captured by the initial divide. Upon capture, the plateau erodes via headward erosion. The amount of divide amplification and migration is increased compared to Regime 1.

Regime 3 *(Perturbation Dominates (Fig. 4.C, Supplemental Movie M3)).* Similar to Regime 2, the perturbation forms a new ridge and upstream local minimum that uplifts as a plateau. However, headward erosion is unable to degrade the ridge before the plateau reaches the same elevation as the initial divide. The perturbation captures the initial ridge, forming a knickpoint that migrates towards the perturbation and amplifies it. The divide then migrates back to the center of the domain.

Model behaviors classified above cleanly separate in β–η space (Fig. 3.B). In general, the perturbation forms a new ridge when $\beta >\sim 1$, which can be understood from geometry: Transition out of Regime 1 requires the maximum elevation of the perturbation on the landscape to be larger than the elevation of the initial channel at the upstream edge of the perturbation:

$$z_P(x_Z) > z_0(x_P - R_P), \tag{14}$$

where $z_P(x_Z)$ is the elevation and location of the highest perturbed topography (Fig. 2.B)

$$z_P(x_Z) = \max[z_0(x) + u(x, t_P)t_P], \qquad x_P - R_P \le x \le x_P. \tag{15}$$

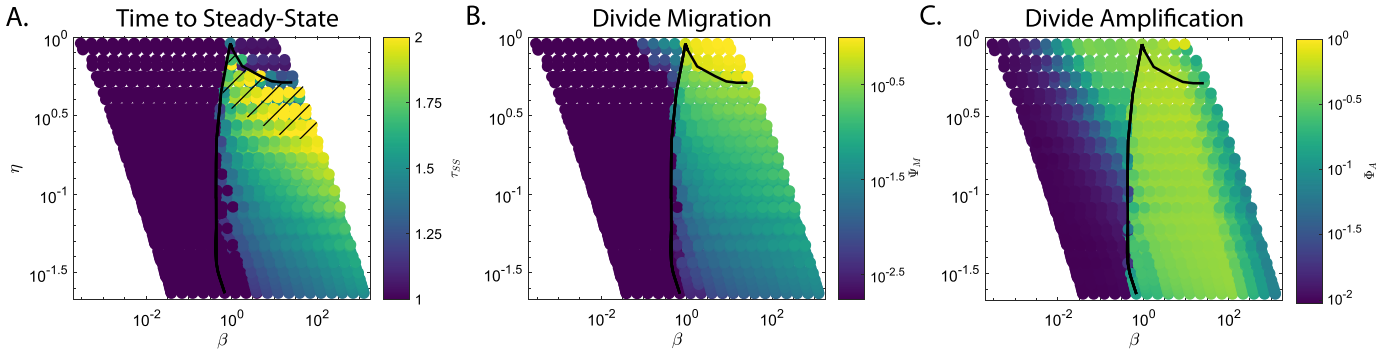

Fig. 5. 1D model regime diagrams as in Fig. 3, with colors corresponding to nondimensional metrics defined in text. Black lines show model regime boundaries. A: Time to steady state, scaled by the longest of channel advection or ridge migration timescales (τ_{SS}). Hatched zone represents models in Regime 2 where divide migration becomes dominant timescale. B: Maximum ridge migration from steady state scaled by perturbation center location within the basin (Ψ_M). C: Maximum ridge amplification relative to steady state scaled by the maximum model topographic deviation from steady state through time (Φ_A).

The perturbation dominates for large β and η. Transition from Regime 2 to Regime 3 can be predicted analytically by comparing the initial divide elevation to the maximum amount of background uplift during the time taken for a wave to travel from the local minimum to the perturbation peak. Regime 2 occurs if

$$z_0(0) > z_0(x_P - R_P) + u_0 T_W, \tag{16}$$

where T_W is the erosive signal transit time from the local minimum to the top of the perturbation (Fig. 2.B):

$$T_W = \int_{R_P + x_Z - x_P}^{x_c} \frac{dx}{C_I(x)} + T_D$$
$$= \frac{(R_P + x_Z - x_P)^{1-HM} - (x_c)^{1-HM}}{k(k_a)^M(1-HM)} + T_D, \tag{17}$$

and T_D is the hillslope diffusion timescale (Fig. 2.B)

$$T_D = \frac{(x_c)^2}{D}. \tag{18}$$

Regime transitions predicted by these analytic values compare well with numerical model results (Fig. 3.B, dashed lines). Discrepancies between analytic and numerical regime boundaries are attributed both to neglecting erosion in the analytic predictions and the spatial grid resolution of the numerical models (Supplemental Methods).

3.1.1. Time to steady state

We assume the landscape is in steady state when topography does not change in time, which is also a steady state in sediment flux in our model (Willett and Brandon, 2002). Time until the profile reestablishes steady state is a predictive metric for transient response. It has been proposed that the transit time of advective kinematic waves in (6) controls this timescale (Whipple and Tucker, 1999; Royden and Perron, 2013).

However, in our simulations, kinematic wave transit competes with drainage divide migration, at speed $C_R(t)$, to set the timescale of landscape adjustment. We compute the time to steady state (T_{SS}) numerically as the time elapsed between $t = 0$ and when the primary drainage divide has migrated to within a small fraction of the initial position (for numerical efficiency, see Supplemental Methods). We then compare T_{SS} with a characteristic erosion time after any local minima have eroded, defined by

$$T_{x_P} = \max\left(T_{C_R}, T_{C_I}\right), \tag{19}$$

where T_{C_R} is the ridge migration timescale and T_{C_I} is the advection time between the perturbation center and channel head of the initial divide (Fig. 2.B)

$$T_{C_I} = \int_{x_P}^{x_c} \frac{dx}{C_I(x)}. \tag{20}$$

T_{C_R} is computed numerically as the time between when any local minima have eroded and when the ridge is at its final steady-state position. Because Regime 1 does not involve local minima formation, T_{C_R} is zero according to this definition (although some ridge migration does occur).

Nondimensional time to steady state is then $\tau_{SS} = T_{SS}/T_{x_P}$, near unity if either channel or ridge transit time approaches T_{SS}. This scaling captures the effect of the 'Divide Migration Number' proposed by Whipple et al. (2017a) (Supplemental Fig. S4), indicating in a simple way when either channels or ridges clearly dominate landscape transient response.

We find this scaling explains the three transient regimes in our 1D simulations (Fig. 5.A). In Regime 1, $\tau_{SS} \approx 1$, as the steady-state timescale is controlled by T_{C_I}. In Regime 2, steady state is still dominantly controlled by T_{C_I}, but τ_{SS} increases beyond 1 with increasing β and η, as T_{C_R} begins influencing response time. As η increases in Regime 2, γ also begins influencing time to steady state with lower γ causing T_{C_R} to sometimes become the dominant timescale (hatched zone of Fig. 5.A; Supplemental Fig. S4). In Regime 3, divide migration is slow compared to channel adjustment and so again $\tau_{SS} \approx 1$, but here T_{C_R} dominates response (Supplemental Fig. S4).

3.1.2. Maximum divide migration

Uplift perturbations induce transient lateral response of the initial drainage divide. We define the maximum amount of divide migration (L_M) by the difference between the maximum length of the unperturbed basin and the initial basin length. We scale this value by the perturbation center location

$$\Psi_M = \frac{L_M}{x_P}, \tag{21}$$

as this represents the maximum horizontal distance the divide can be perturbed.

In all regimes, higher β and η correspond to higher Ψ_M, with a distinct break occurring at the Regime 1 boundary (Fig. 5.B). In Regime 1, divide migration is negligible compared to perturbation position for all except the highest β and η. Mudd and Furbish (2005) analyzed this behavior in detail to show differences in channel incision across hillslopes cause the divide to migrate

toward lower erosion rates. Here, the concave knickpoint induces lower slopes as it propagates to the hillcrest, thus lowering local erosion rates of the perturbed basin and causing the divide to migrate towards the perturbation.

Regime 2 exhibits larger degrees of ridge migration, and shows the trade off between perturbation relief, size, and position in affecting the ridge. η can be approximated as R_P/x_P, such that low η values represent small perturbations near the channel base. In such scenarios, even if a perturbation creates large relief (high β), its proximity to base level means that headward erosion reaches the ridge before the upstream plateau reaches the initial divide. As η increases in Regime 2, plateaus that capture the perturbation have higher relief. Higher relief of the upstream channel, and larger amount of time needed to erode the perturbation after it initially uplifts, result in larger divide migration (Mudd and Furbish, 2005).

Regime 3 corresponds to perturbations that have sizes approximately equal to the distance from divide ($\eta \approx 1$). Although these perturbations have the largest amounts of scaled ridge disruption, Ψ_M is less than 1 such that the maximum transient divide position never corresponds to the location of maximum uplift. This results from the initial channel topography, which offsets maximum perturbed topography from the perturbation center (x_Z in equation (17)).

3.1.3. Maximum divide amplification

Uplift perturbations also drive transient amplification of drainage divide elevations when the perturbation signal propagates up channels to the divide. We quantify vertical divide disruption by measuring the maximum amount of divide amplification (Z_A) compared to the maximum topographic deviation from steady state anywhere within the profile at any time

$$\Phi_A = \frac{Z_A}{\max(|z(x,0) - z(x,t)|)}. \tag{22}$$

Vertical disruption is not monotonic with β and η (Fig. 5.C). In Regime 1, although the channel response is limited to knickpoint propagation, perturbations induce increasing ridge amplification with higher β and η. Perturbations that form higher relief and occur closer to the divide produce larger transient signals that persist as they propagate upstream (Mudd and Furbish, 2005).

A clear increase in Φ_A occurs at the Regime 1 boundary, but Regimes 2 and 3 are indistinguishable. Rather, increasing β results in decreasing Φ_A. This zone of Φ_A, which is largely independent of η, is controlled by the amount of relief, relative to the perturbation, that the uplifting plateau can generate before its adjacent ridge is captured and it is propagated upstream as a knickpoint to the dominant divide. For $\beta \approx 10^1$, the uplifting plateau captures the perturbation by generating a higher-relief landform than the initial perturbation relief ($u_P t_P$). Conversely, for $\beta > \approx 10^2$, the incision wave associated with channel beheading is able to propagate from base level to the initially high-relief perturbation and erode it before the plateau uplifts to the height of the ridge, thus forming a relatively lower-relief knickpoint compared to the perturbation relief. This metric thus distinguishes whether the perturbation or the subsequent basin disruption is the dominant feature that drives divide transience

3.2. 2D models

In real landscapes, localized uplift is observed to generate lateral channel migration (Perkins et al., 2016) and spatially variable ridge migration (Willett et al., 2014). Such complex behavior is not possible in 1D, but can arise in 2D models.

We do not attempt a complete characterization of transient response to localized uplift in 2D, but use a coarse grid search to demonstrate that 2D models exhibit broadly similar transient landscape adjustment to localized uplift as 1D models. Models with low β and η generate negligible landscape response. As β and η increase, disruption magnitude also increases. However, there is also significant additional complexity in 2D, due to the additional spatial degree of freedom.

Most significant transient adjustments to localized uplift are spatially anisotropic (Fig. 6, upper-left panel of Supplemental Movie M4). Model channels with high drainage areas, although initially beheaded by the perturbation, often retain their original configuration in the new steady state (Whipple et al., 2017b). Low drainage area channels, however, are influenced by the perturbation and reorganize to form radial drainages that persist into the new steady state. We do not attempt to constrain pre-existing channel sizes that remain stable to perturbations, as numerical landscape evolution models are known to be more stable to lateral channel migration than real landscapes (Goren et al., 2014).

Plateaus form upstream of the perturbation in response to channel beheading, mechanistically similar to that proposed to occur by tectonically-driven stream capture (Yang et al., 2015). Finally, ridge migration is spatially localized upstream from the perturbation (Fig. 6). All models that experience basin adjustment do not evolve back to the initial network geometry, but adopt a new configuration of channels and ridges which balance background uplift and erosion everywhere.

3.2.1. Fragility of steady-state solutions in 2D

Occurrence of different steady-state solutions before and after transient uplift suggests that 2D topographic steady states are unstable to sufficiently large perturbations. Drainage divide response demonstrates a systematic metric of change. We measure the maximum amount of divide migration (L_M) and the affected initial divide length (L_D) at initial and final steady state by calculating the Euclidean distance between every point of the longest continuously differing divide sections (Fig. 7.A). L_M is defined as the maximum distance between nearest neighbor points in initial versus final steady state (Fig. 7.A, solid red line). L_D is calculated as the summed Euclidean distance along the initial, unmatched divide section (Fig. 7.A, dashed red line). Both metrics are nondimensionalized by the Hack's Law distance ($x_H = (A(x_P, y_P)/k_a)^{1/H}$) between perturbation center and the initial upstream divide ($\Psi_M = L_M/x_H$, equivalent to equation (21) in 1D; $\Psi_D = L_D/x_H$, which has no 1D analogue).

Ψ_M and Ψ_D capture the magnitude and extent of divide migration, but do not quantify channel network topology associated with basin area change. Thus, we calculate the basin areal difference, on a pixel-by-pixel basis, between initial and final steady states. This change is measured by the basin Jaccard distance (Jaccard, 1901) defined as

$$d_B = 1 - J(B_I, B_F) = 1 - \frac{|B_I \cap B_F|}{|B_I| + |B_F| - |B_I \cap B_F|}, \tag{23}$$

where $J(B_I, B_F)$ is the Boolean Jaccard similarity index between the initial (B_I) and final (B_F) sets of model catchment pixels; $|B_I|$ is the total number of perturbed-basin pixels in the initial topography, $|B_F|$ is the total number in the final topography, and $|B_I \cap B_F|$ is the number of pixels that exist in both states (Fig. 7.A, shaded regions). Values of d_B closer to 1 correspond to greater dissimilarity between model domains.

We find that low β and η produce negligible disruption (we impose a threshold of 2 altered pixels to register a signal) between states (Fig. 7). Ψ_M and Ψ_D increase with increasing β and η, suggesting perturbation locations control the extent of drainage divide response, and overall stability of the initial steady state. Maximum response magnitudes are always less than the distance between

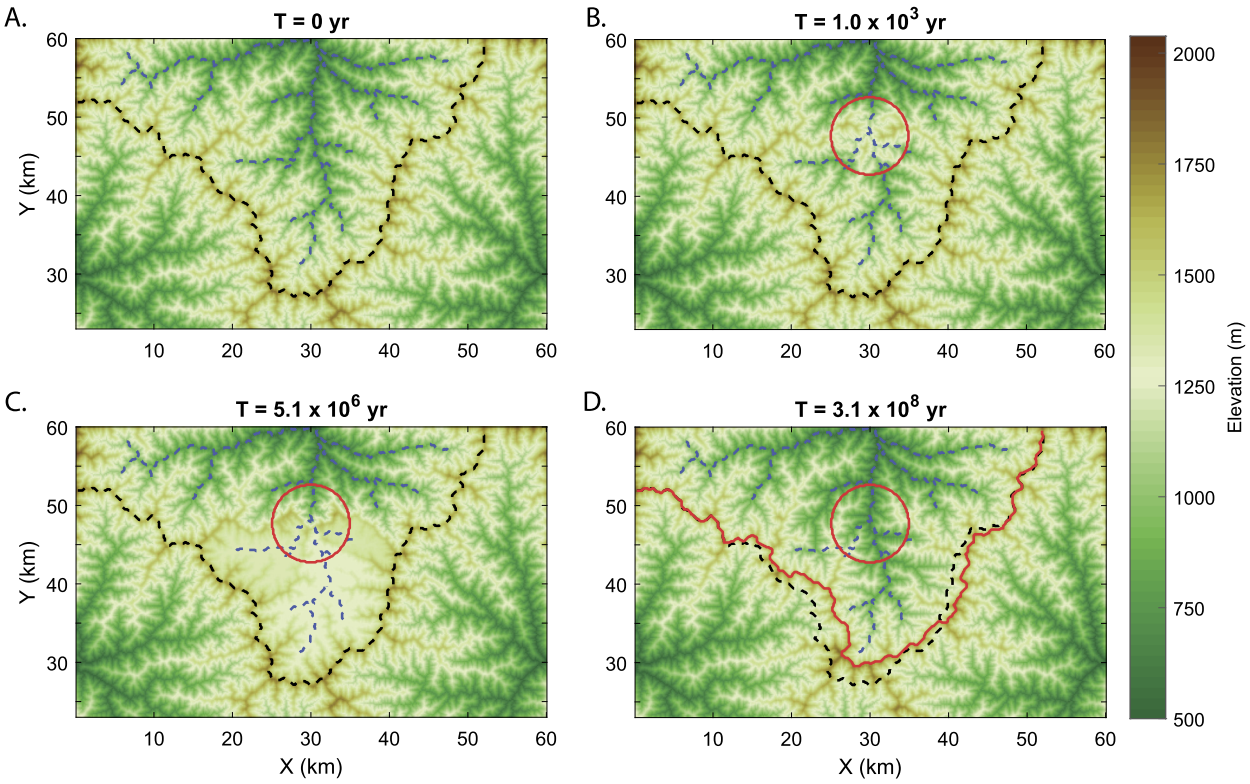

Fig. 6. 2D model exhibiting Regime 3 behavior, plotting the upper half of the model domain. Dashed black and blue lines represent initial divide locations and river channel positions, respectively. Red circles represent perturbation boundary within landscape. Solid red line indicates final steady-state divide location. Panel titles indicate model times at (A) initial steady-state topography; (B) after perturbation uplift has ended; (C) transient topography showing upstream plateau uplift; and (D) final steady-state topography.

the perturbation and divide, but ridges always migrate towards the perturbation (similar to the 1D behavior).

The Jaccard distance d_B shows a similar pattern (Fig. 7.D), and captures an important difference to 1D model results: in 2D, localized transient uplift perturbations cause significant and distributed disruption even after completion of the perturbation and the landscape has adjusted back to topographic steady state. Maximum d_B for the 25 simulations we show here is 0.16, which represents 16.9% area adjustment of the perturbed basin between initial and final steady states. This value corresponds to a perturbation size (as a fraction of initial basin size) of 32.4%, and an adjusted basin area to perturbation area ratio of 0.52. Across all models, this ratio ranges from 0.002 to 8.2.

Furthermore, we observe model behaviors that are qualitatively-analogous to the 1D model regimes again separate in the nondimensional parameter space (Fig. 7.B–D, borders). Low β and η values generate Regime 1 behaviors defined by no plateau formation and minimum disruption (black borders). Mid-ranged values follow Regime 2, where the perturbation creates plateaus that are subsequently dissected by the perturbed basin's main channel when the perturbation erodes (gray borders). Finally, high β and η cause Regime 3 behavior where plateaus persist until they are dissected on all sides by the surrounding basins, causing a large degree of divide migration (red borders).

3.2.2. Transient topographic adjustment

Landscape disruption also occurs transiently during and after the uplift perturbation. As with 1D models, we observe a landscape evolution that involves knickpoints and plateau formation. We also observe lateral internal channel reorganization that is not possible in 1D models. To illustrate the effect of single perturbation parameters on topographic adjustment through time, we calculate a topographic derivation d_t between the initial steady state $z(x, y, 0)$ and time-varying elevations $z(x, y, t)$ as

$$d_t = 1 - \frac{|z(x, y, 0) \cap z(x, y, t)|}{|z(x, y, 0)|}, \tag{24}$$

limited to grid cell differences less than 5% topographic change from the initial state. Thus, $|z(x, y, 0)|$ is the total number of model grid cells and $|z(x, y, 0) \cap z(x, y, t)|$ is the total number of grid cells where $|z(x, y, 0) - z(x, y, t)| / z(x, y, 0) < .05$ (upper-right panel of Supplemental Movie M4).

Fig. 8 illustrates the difference in transient landscape response to local perturbation disruption between Regime 2 and 3 behaviors. Regime 2 response is characterized by non-monotonic increases in d_t through time (Fig. 8.A). Rather, d_t initially increases when local minima upstream of the perturbation uplift as a plateau; followed by a decrease in d_t as the perturbation and plateau are eroded by the perturbed-basin channels; and finally small increases in d_t as the landscape adjusts to minor disequilibrium. Conversely, Regime 3 response is characterized by a monotonic increase in d_t as the perturbation creates a plateau that continuously uplifts until it is dissected by the surrounding basins (Fig. 8.B–C, red lines; bottom panel of Supplemental Movie M4).

Fig. 8 also demonstrates parameter dependencies that are convolved through the nondimensional η and β. We see that perturbations forming close to the divide have smaller initial influence on topographic change than those from further down the basin, which are able to affect more upstream sub-catchments (Fig. 8.A); however, long-term adjustments are equivalent. Similarly, low uplift rates are less disruptive compared to higher rates (Fig. 8.B), consistent with geometric predictions from 1D (Fig. 3). Finally, the amount of disruption increases with greater radii (Fig. 8.C), as larger perturbations are able to influence neighboring sub-basins within the landscape. Generally, perturbation size and uplift rate

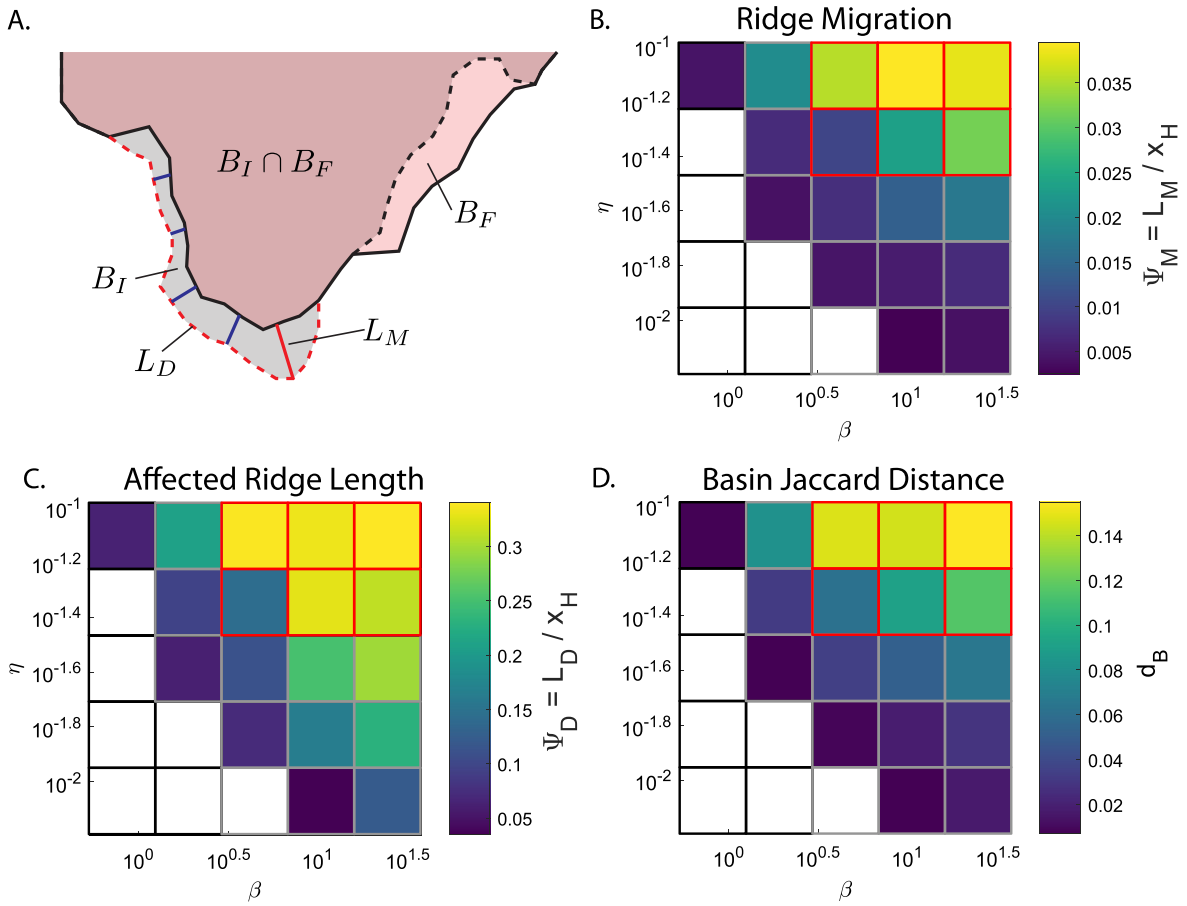

Fig. 7. Regime diagrams for a grid search of 25 2D models. Colored panels correspond to specific nondimensional metrics between initial and final steady states, with borders representing model behavior regimes (black is Regime 1, gray is Regime 2, red is Regime 3), as described in the text. White panels exhibit no change between initial and final steady states. A: Metric schematic, shaded areas are initial and final perturbed basin, dashed lines are initial basin divide, and solid black line is final basin divide. Blue lines are shortest distance between initial and final ridge points, with solid red line being the longest distance (L_M). Dashed red line represents longest segment of initial divide that is separated from the final (L_D). B: Maximum divide migration (L_M, solid red line of A), scaled by Hack's Law distance to divide (x_H). C: Length of initial divide that experienced migration (L_D, red dashed line of A), scaled by Hack's Law distance to divide. D: Jaccard distance d_B (equation (23)) between initial and final pixels of the perturbed basin (shaded regions of A).

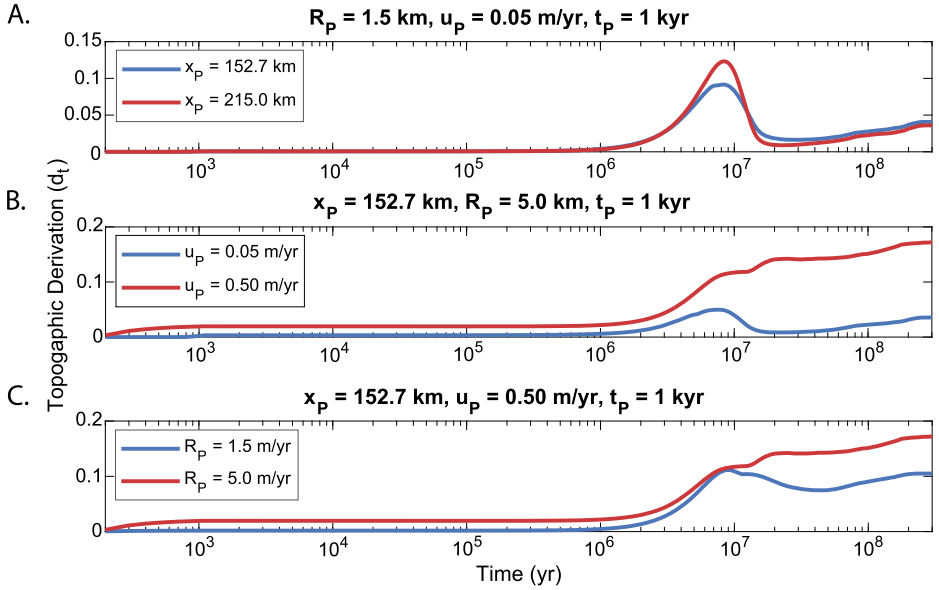

Fig. 8. Transient topographic distance d_t through time for 2D models, panels represent differences in a single parameter. A: Differences in perturbation location (x_P). B: Differences in maximum perturbation uplift rate (u_P). C: Differences in perturbation radius (R_P).

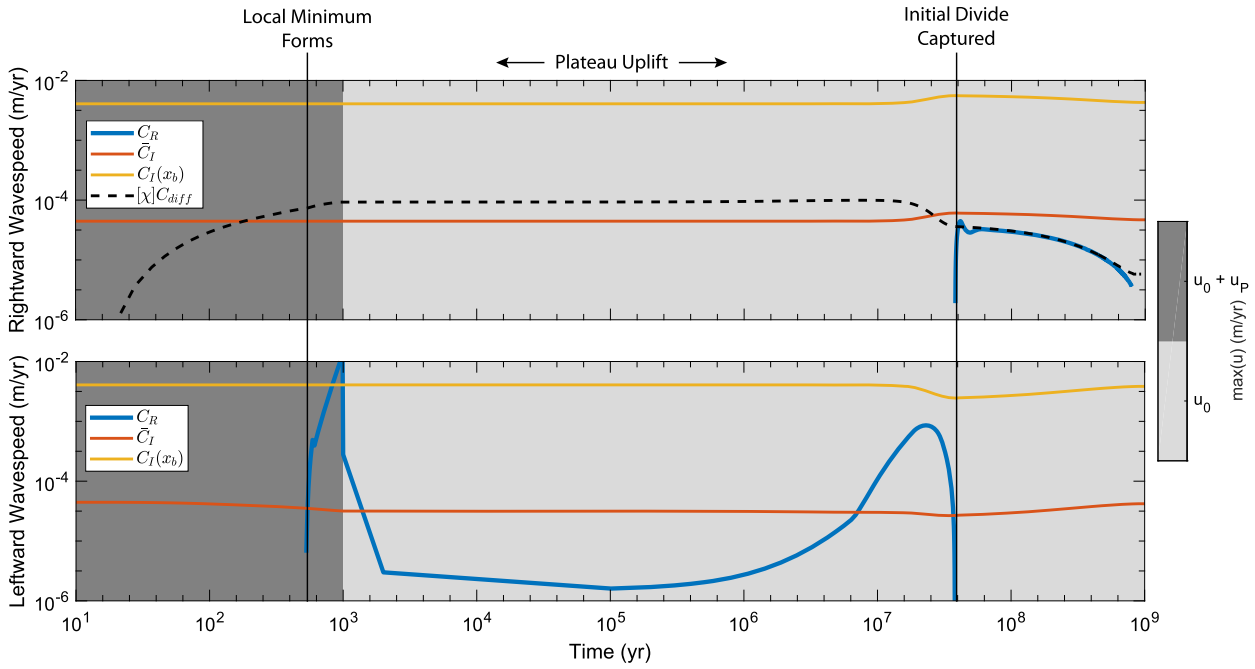

Fig. 9. Rightward (top panel) and leftward (bottom panel) 1D model wave speeds through time for Regime 3 model with parameters: $u_P = 5.6$ m/yr, $t_P = 1000$ yr, $R_P = 13.3$ km, $x_P = 16.7$ km. Blue lines represent main divide migration speeds (C_R). Dashed line is divide migration speed from equation (26). Red and yellow lines are mean ($\bar{C}_I$) and maximum ($C_I(x_b)$) channel wave speeds. Panel shading is by maximum uplift rate in the domain.

are the most important parameters determining subsequent landscape response.

4. Discussion

Landscapes respond to perturbations that occur on a wide range of spatial and temporal scales. We analyze spatially localized, transient uplift perturbations and find they can affect landscapes nonlocally: the scale of landscape response to a particular size and location of disruption extends well beyond the perturbation. This behavior is distinct from landscape adjustment to large-scale climate or tectonics, and may be important for determining transient histories in terrain that regularly experiences local disruptions.

In both 1D and 2D models, transient topographic response to localized perturbations include plateau formation by channel beheading and divide migration. Previous studies have characterized such topographic measures of transience through the lens of fluvial channel profiles (e.g. Kirby and Whipple, 2001; Royden and Perron, 2013; Willett et al., 2014) or hillslopes (e.g. DiBiase et al., 2012; Hurst et al., 2013). Here, we show the integration of both process classes demonstrates distinct regimes of fluvial versus hillslope control.

Landscape transient response to uplift perturbations is controlled by a competition between kinematic wave propagation that transmits information about uplift and erosion perturbations up fluvial channels, and migration of drainage divides that separate domains of fluvial incision with lateral erosion velocities of opposite sign. These two wave-like adjustments occur on vastly different timescales, and vary strongly in space according to Hack's Law.

We analyze the competition between these two timescales for a Regime 3 1D model in Fig. 9 (parameters in caption). We plot the maximum (yellow lines) and spatially-averaged (red lines) channel wavespeeds in the left and right basins along with the numerically-evaluated drainage divide migration speed (blue line). We see that the perturbation experiences leftward ridge migration as soon as it forms. When the initial drainage divide is captured by the perturbation, ridge migration direction switches and the model relaxes back to steady state.

Divide migration velocity C_R is determined by the difference in erosion rates on either side of a ridge (Mudd and Furbish, 2005). However, nonlocal and spatially variable geomorphic transport laws in the vicinity of ridges make calculating ridge velocity challenging. A solution to this is the dimensionless transformed version of the downstream distance x suggested by Royden and Perron (2013), defined (for constant erodibility K) as

$$\chi = \frac{1}{h_0} \int_{x_b}^{x_c} \left(\frac{A_0}{A(x)} \right)^M dx, \tag{25}$$

where h_0 and A_0 are a reference elevation and drainage area, respectively. Willett et al. (2014) propose that the jump in χ evaluated across a drainage divide, $[\chi] = \chi_R - \chi_L$ for χ_R calculated from (25) in the right basin, and χ_L calculated in the left basin, predicts the direction of ridge migration.

We find that, scaling $[\chi]$ by the rate of soil diffusion that controls transient response for $x < x_c$, ridge migration direction and magnitude can be predicted (black dashed line in Fig. 9). When non-uniform uplift is absent, as in the final transient evolution of 1D models, ridge velocity is

$$C_R = [\chi]\, C_{diff}, \tag{26}$$

where $C_{diff} = D/x_c$ is a hillslope linear diffusion speed with x_c given by equation (9). We let $h_0 = 1$ m and determine A_0 empirically to be 0.09 m^2 for our simulations. This method of using the difference between the integrated channel profiles differs from that derived by Braun (2018) based on local channel head slopes.

Equation (26) suggests that differences in fluvial erosion across a divide alone is insufficient for predicting divide migration. Although we do not explicitly focus on the mechanics of hillslope processes, hillslope-channel coupling through ridge migration affects global aspects of model landscape response. Fig. 10 shows time evolution of three Regime 3 1D models, identical to that in Fig. 9 except for the value of D. We see that, although the early stages of landscape response dominated by transient uplift and

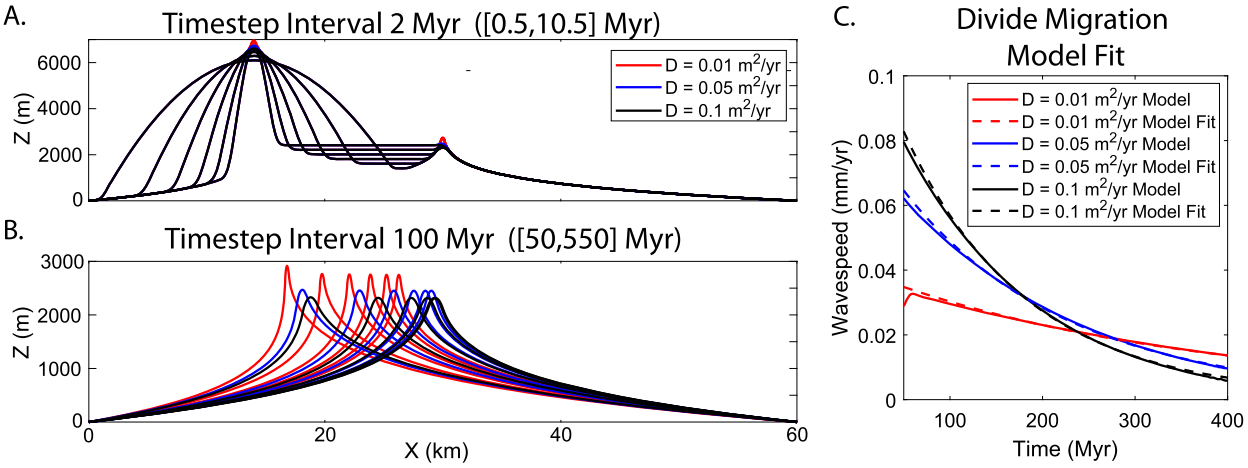

Fig. 10. Regime 3 models with same parameters as Fig. 9, but for different values of soil diffusivity (D). (A) Model topography during localized uplift and plateau formation. (B) Ridge migration after local minima have eroded. (C) Main drainage divide rightward migration rates of model (solid lines) and fits from equation (26) (dashed lines) over timescales described in panel B. Comparable to upper-panel of Fig. 9, after initial divide has been captured.

plateau formation are nearly identical, later stages of ridge migration vary significantly both in rate of adjustment and transient divide height. As demonstrated by Fig. 10.C, C_R as calculated by equation (26) accurately predicts the rate of ridge migration in each case. This provides an integrated physical interpretation of ridge migration velocity hypothesized by Whipple et al. (2017a) on the basis of 2D simulations and single-basin 1D models. Both knickpoint advection and hillslope soil transport play a major role in setting divide stability and migration rates (Fig. 9, equation (26)).

We observe that localized uplift acts as a lens for upstream divides, both vertically amplifying (Fig. 5.C) and laterally advecting ridges towards the perturbation (Fig. 6). This behavior is distinct from perturbations that cause all drainage divides to migrate, as in response to a gradient in forcing imposed across the entire landscape (Bonnet, 2009; Willett et al., 2014). Although not analyzed explicitly, divide transience should also manifest in neighboring basin divides not shared with the perturbed basin, as changes in drainage area induce an erosional response in all downstream channels (Willett et al., 2014).

The results of our 1D and 2D models provide a new conceptual approach to inferring erosional histories from current topographic state. Although this study focused on perturbations formed by transient bedrock uplift, our results may also apply to other topographic perturbations. Large landslides can dam channel valleys on 1–100,000 yr timescales, creating local minima that stretch 1–100's of kilometers upstream (e.g. Mackey et al., 2011), within the range of scales explored here. Although these perturbations are short-lived, a quiescence of erosion upstream of the landslide would induce behavior similar to that observed in Regime 2 – small amounts of upstream divide amplification and migration towards to the perturbation before incision by dam-breaching. Similarly, slow moving landslides and earthflows can provide locally higher sediment loads that modulate channel incision (Egholm et al., 2013), creating knickpoints similar to our Regime 1 models.

Other environments relevant to this study are continental magmatic landscapes, where localized and episodic uplift via intrusions and eruptions is common. For example, the Colorado Plateau, USA, contains numerous Oligocene laccolith groups that were emplaced on previously lower-relief topography (Gilbert, 1877). Our results suggest that sufficiently large-amplitude localized uplift will reorganize small catchments into radial drainage patterns, but pre-existing fluvial channels with large drainage areas may persist in time. Thus, drainage patterns surrounding these laccolith groups could encode the prior landscape form and rate of magmatic uplift through time on the Colorado Plateau.

The Cascades volcanic arc, USA, provides another example, where subduction-related tectonic uplift and a rain shadow-induced precipitation gradient are present. However, uplift perturbations in the form of volcanic edifices, lava flows, ash deposits (Hildreth, 2007), landslides (Pierson, 2009), and intrusion-related surface deformation (likely prevalent although poorly documented except in special cases, e.g., Wicks et al., 2002) are common. Within this complex environment, signatures of landscape evolution are difficult to diagnose, but our analyses suggest predictions to test.

For example, the dichotomy between high, relatively undissected High Cascades topography is often posited to reflect differences in hydrology that controls the efficiency of fluvial erosion (e.g., Jefferson et al., 2010). However, we have shown beheading of channels by magmatic intrusions can also produce plateau-like provinces. Likewise, although the main Cascades drainage divide is approximately parallel to the subduction zone, along-arc divide variations and downstream channel patterns reflect interplay between local volcanic disruptions, background tectonics, and erosion within the context of this model. Landscape evolution in volcanic terrains is poorly constrained compared to other tectonic environments (Karlstrom et al., 2018), but we see an opportunity to use topographic form to infer long-term magmatic as well as erosional patterns.

5. Conclusion

We conclude by revisiting the problem posed by a spectrum of landscape perturbations at a range of length scales (Fig. 1). Past studies have analyzed landscape response to large-scale processes such as tectonics, climate, and mantle upwelling. We analyze the effects of meso-scale uplift perturbations to landscape evolution, finding a spatially distributed and long-lasting topographic response.

Using 1D and 2D models, we find that localized uplift perturbations often induce divide migration and amplification, with magnitude of response dependent on dimensionless ratios that relate perturbation size and emplacement rate to pre-existing topographic state. Divide migration rates depend both on channel advection and hillslope transport processes, and the regime of landscape response is largely determined by the ratio of knickpoint propagation to divide adjustment via hillslope processes. Perturbations can also form local minima that evolve into large, upstream

plateaus. In both 1D and 2D models, localized uplift acts as a lens that causes ridges upstream of the perturbation to migrate towards the perturbation. In 2D models, perturbations can cause a permanent shift in the steady-state configuration of channels and ridges, the pattern of which relates both to pre-existing topographic form and scale of the localized uplift.

Acknowledgements

The authors would like to thank E.D. Humphreys, E.A. Lamont, P.R. Richardson, and D.R. Toomey for thoughtful discussion which contributed to this work. Comments contributed by editor J.-P. Avouac, S.M. Mudd, and one anonymous reviewer enhanced the quality of this manuscript. This work was supported by NSF GRF 1309047 awarded to D.O.

Appendix A. Supplementary material

Supplementary material related to this article can be found online at https://doi.org/10.1016/j.epsl.2018.11.006.

References

Anderson, R.E., Eargle, D.H., Davis, B.O., 1973. Geologic and Hydrologic Summary of Salt Domes in Gulf Coast Region of Texas, Louisiana, Mississippi, and Alabama. Technical Report. Geological Survey, Denver, CO, USA.

Black, B.A., Perron, J.T., Hemingway, D., Bailey, E., Nimmo, F., Zebker, H., 2017. Global drainage patterns and the origins of topographic relief on Earth, Mars, and Titan. Science 356, 727–731.

Bonnet, S., 2009. Shrinking and splitting of drainage basins in orogenic landscapes from the migration of the main drainage divide. Nat. Geosci. 2, 766–771.

Braun, J., 2018. A review of numerical modeling studies of passive margin escarpments leading to a new analytical expression for the rate of escarpment migration velocity. Gondwana Res. 53, 209–224.

Braun, J., Willett, S.D., 2013. A very efficient O(n), implicit and parallel method to solve the stream power equation governing fluvial incision and landscape evolution. Geomorphology 180, 170–179.

Braun, J., Robert, X., Simon-Labric, T., 2013. Eroding dynamic topography. Geophys. Res. Lett. 40, 1494–1499.

Castro, J.M., Cordonnier, B., Schipper, C.I., Tuffen, H., Baumann, T.S., Feisel, Y., 2016. Rapid laccolith intrusion driven by explosive volcanic eruption. Nat. Commun. 7, 13585.

Corry, C.E., 1988. Laccoliths: Mechanics of Emplacement and Growth, vol. 220. Geological Society of America.

DiBiase, R.A., Heimsath, A.M., Whipple, K.X., 2012. Hillslope response to tectonic forcing in threshold landscapes. Earth Surf. Process. Landf. 37, 855–865.

Duvall, A.R., Tucker, G.E., 2015. Dynamic ridges and valleys in a strike-slip environment. J. Geophys. Res., Earth Surf. 120, 2016–2026.

Egholm, D.L., Knudsen, M.F., Sandiford, M., 2013. Lifespan of mountain ranges scaled by feedbacks between landsliding and erosion by rivers. Nature 498, 475.

Gilbert, G.K., 1877. Report on the Geology of the Henry Mountains. US Government Printing Office.

Goren, L., Willett, S.D., Herman, F., Braun, J., 2014. Coupled numerical–analytical approach to landscape evolution modeling. Earth Surf. Process. Landf. 39, 522–545.

Guzzetti, F., Ardizzone, F., Cardinali, M., Rossi, M., Valigi, D., 2009. Landslide volumes and landslide mobilization rates in Umbria, central Italy. Earth Planet. Sci. Lett. 279, 222–229.

Hack, J.T., 1957. Studies of Longitudinal Stream Profiles in Virginia and Maryland. US Government Printing Office, Washington, DC, USA.

Harel, M.-A., Mudd, S., Attal, M., 2016. Global analysis of the stream power law parameters based on worldwide 10 Be denudation rates. Geomorphology 268, 184–196.

Hildreth, W., 2007. Quaternary Magmatism in the Cascades: Geologic Perspectives. 1744. US Geological Survey.

Hurst, M.D., Mudd, S.M., Yoo, K., Attal, M., Walcott, R., 2013. Influence of lithology on hillslope morphology and response to tectonic forcing in the northern Sierra Nevada of California. J. Geophys. Res., Earth Surf. 118, 832–851.

Jaccard, P., 1901. Étude comparative de la distribution florale dans une portion des Alpes et des Jura. Bull. Soc. Vaud. Sci. Nat. 37, 547–579.

Jefferson, A., Grant, G., Lewis, S., Lancaster, S., 2010. Coevolution of hydrology and topography on a basalt landscape in the Oregon Cascade Range, USA. Earth Surf. Process. Landf. 35, 803–816.

Karlstrom, L., Richardson, P.W., O'Hara, D., Ebmeier, S.K., 2018. Magmatic landscape construction. J. Geophys. Res., Earth Surf. 123, 1710–1730. https://doi.org/10.1029/2017JF004369.

Kirby, E., Whipple, K., 2001. Quantifying differential rock-uplift rates via stream profile analysis. Geology 29, 415–418.

Lague, D., 2014. The stream power river incision model: evidence, theory and beyond. Earth Surf. Process. Landf. 39, 38–61.

Larsen, I.J., Montgomery, D.R., 2012. Landslide erosion coupled to tectonics and river incision. Nat. Geosci. 5, 468–473.

Mackey, B.H., Roering, J.J., Lamb, M.P., 2011. Landslide-dammed paleolake perturbs marine sedimentation and drives genetic change in anadromous fish. Proc. Natl. Acad. Sci. 108, 18905–18909.

Molnar, P., England, P., 1990. Late Cenozoic uplift of mountain ranges and global climate change: chicken or egg? Nature 346, 29–34.

Mudd, S.M., Furbish, D.J., 2005. Lateral migration of hillcrests in response to channel incision in soil-mantled landscapes. J. Geophys. Res., Earth Surf. 110.

Perkins, J.P., Finnegan, N.J., Henderson, S.T., Rittenour, T.M., 2016. Topographic constraints on magma accumulation below the actively uplifting Uturuncu and Lazufre volcanic centers in the Central Andes. Geosphere 12, 1078–1096.

Perron, T.J., Fagherazzi, S., 2012. The legacy of initial conditions in landscape evolution. Earth Surf. Process. Landf. 37, 52–63.

Perron, J.T., Kirchner, J.W., Dietrich, W.E., 2009. Formation of evenly spaced ridges and valleys. Nature 460, 502.

Pierson, T.C., 2009. InSAR detection of renewed movement of a large ancient landslide in the Columbia River Gorge, Washington. In: 2009 Portland GSA Annual Meeting.

Pollard, D.D., Johnson, A.M., 1973. Mechanics of growth of some laccolithic intrusions in the Henry Mountains, Utah, II: bending and failure of overburden layers and sill formation. Tectonophysics 18, 311–354.

Roering, J.J., Kirchner, J.W., Dietrich, W.E., 2001. Hillslope evolution by nonlinear, slope-dependent transport: steady state morphology and equilibrium adjustment timescales. J. Geophys. Res., Solid Earth 106, 16499–16513.

Royden, L., Perron, T.J., 2013. Solutions of the stream power equation and application to the evolution of river longitudinal profiles. J. Geophys. Res., Earth Surf. 118, 497–518.

de Saint-Blanquat, M., Habert, G., Horsman, E., Morgan, S.S., Tikoff, B., Launeau, P., Gleizes, G., 2006. Mechanisms and duration of non-tectonically assisted magma emplacement in the upper crust: the Black Mesa pluton, Henry Mountains, Utah. Tectonophysics 428, 1–31.

Seidl, M., Dietrich, W., 1992. The problem of channel erosion into bedrock. Funct. Geomorph. 23, 101–124.

Shen, X., Anagnostou, E.N., Mei, Y., Hong, Y., 2017. A global distributed basin morphometric dataset. Sci. Data 4, 160124.

Stock, J.D., Montgomery, D.R., 1999. Geologic constraints on bedrock river incision using the stream power law. J. Geophys. Res. B 104, 4983–4993.

Strahler, A.N., 1957. Quantitative analysis of watershed geomorphology. Eos 38, 913–920.

Sweeney, K.E., Roering, J.J., Almond, P., Reckling, T., 2012. How steady are steady-state landscapes? Using visible–near-infrared soil spectroscopy to quantify erosional variability. Geology 40, 807–810.

Sweetkind, D.S., Blackwell, D.D., 1989. Fission-track evidence of the Cenozoic thermal history of the Idaho batholith. Tectonophysics 157, 241–250.

Tucker, G.E., Bras, R.L., 1998. Hillslope processes, drainage density, and landscape morphology. Water Resour. Res. 34, 2751–2764.

Whipple, K.X., Tucker, G.E., 1999. Dynamics of the stream-power river incision model: implications for height limits of mountain ranges, landscape response timescales, and research needs. J. Geophys. Res., Solid Earth 104, 17661–17674.

Whipple, K., Forte, A., DiBiase, R., Gasparini, N., Ouimet, W., 2017a. Timescales of landscape response to divide migration and drainage capture: implications for the role of divide mobility in landscape evolution. J. Geophys. Res., Earth Surf. 122, 248–273.

Whipple, K.X., DiBiase, R.A., Ouimet, W.B., Forte, A.M., 2017b. Preservation or piracy: diagnosing low-relief, high-elevation surface formation mechanisms. Geology 45, 91–94.

Wicks, C.W., Dzurisin, D., Ingebritsen, S., Thatcher, W., Lu, Z., Iverson, J., 2002. Magmatic activity beneath the quiescent Three Sisters volcanic center, central Oregon Cascade Range, USA. Geophys. Res. Lett. 29.

Wilkinson, B.H., McElroy, B.J., Kesler, S.E., Peters, S.E., Rothman, E.D., 2009. Global geologic maps are tectonic speedometers—rates of rock cycling from area-age frequencies. Geol. Soc. Am. Bull. 121, 760–779.

Willett, S.D., 2010. Erosion on a line. Tectonophysics 484, 168–180.

Willett, S.D., Brandon, M.T., 2002. On steady states in mountain belts. Geology 30, 175–178.

Willett, S.D., McCoy, S.W., Perron, J.T., Goren, L., Chen, C.-Y., 2014. Dynamic reorganization of river basins. Science 343, 1248765.

Yang, R., Willett, S.D., Goren, L., 2015. In situ low-relief landscape formation as a result of river network disruption. Nature 520, 526–529.